



Report on field trip to Kiritimati in 2002

‘Photosynthesis versus exopolymer degradation in the formation of microbialites
on the atoll of Kiritimati, Republic of Kiribati, Central Pacific’

published by:

Arp, G., Helms, G., Karlinska, K., Schumann, G., Reimer, A.,

Reitner, J. & Trichet, J.

Geomicrobiology Journal (ms accepted)

2010

Photosynthesis versus exopolymer degradation in the formation of microbialites on the atoll of Kiritimati, Republic of Kiribati, Central Pacific

Gernot Arp^{1*}, Gert Helms^{1†}, Klementyna Karlinska^{1‡}, Gabriela Schumann^{1§},
Andreas Reimer¹, Joachim Reitner¹ and Jean Trichet²

¹ Geowissenschaftliches Zentrum, Universität Göttingen, Goldschmidtstraße 3, D-37077 Göttingen, Germany.

² Laboratoire de Géologie de la Matière Organique, Université d'Orléans, F-45067 Orléans Cedex 2, France.

[†] present address: Klaushöhe 13, D-83471 Berchtesgaden, Germany.

[‡] present address: Department für Geo- und Umweltwissenschaften, Paläontologie & Geobiologie, LMU München, Richard-Wagner-Str. 10, D-80333 München, Germany.

[§] present address: Fraunhofer-Gesellschaft zur Förderung der angewandten Forschung e.V. (FHG), Hansastraße 27 C, D-80686 München, Germany.

Running Title: Microbialite formation on the atoll of Kiritimati

* Corresponding author: G. Arp, Tel.: +49 551 397986; fax: +49 551 397918 53; e-mail:

garp@gwdg.de

Abstract

Aragonitic microbialites, characterized by a reticulate fabric, were discovered beneath lacustrine microbial mats on the atoll of Kiritimati, Republic of Kiribati, Central Pacific. The microbial mats, with cyanobacteria as major primary producers, grow in evaporated seawater modified by calcium carbonate and gypsum precipitation and calcium influx via surface and/or groundwaters. Despite the high aragonite supersaturation and a high photosynthetic activity, only minor aragonite precipitates are observed in the top parts of the microbial mats. Instead, major aragonite precipitation takes place in lower mat parts at the transition to the anoxic zone. The prokaryotic community shows a high number of phylotypes closely related to halotolerant taxa and/or taxa with preference to oligotrophic habitats. Soil- and plant-inhabiting bacteria underline a potential surface or subsurface influx from terrestrial areas, while chitinase-producing representatives coincide with the occurrence of insect remains in the mats. Strikingly, many of the clones have their closest relatives in microorganisms either involved in methane production or consumption of methane or methyl compounds. Methanogens, represented by the genus methylotrophic *Methanohalophilus*, appear to be one of the dominant organisms in anaerobic mat parts. All this points to a significant role of methane and methyl components in the carbon cycle of the mats. Nonetheless, thin sections and physicochemical gradients through the mats, as well as the ^{12}C -depleted carbon isotope signatures of carbonates indicate that (i) spherulitic components of the microbialites initiate in the photosynthesis-dominated orange mat top layer, and further grow in the green and purple layer below. Therefore, these spherulites are considered as product of an extraordinary high photosynthesis effect simultaneous to a high inhibition by pristine exopolymers. (ii) Then, successive heterotrophic bacterial activity leads to a condensation of the exopolymer framework, and finally to the formation of crevice-like zones of partly degraded exopolymers. Here initiation of horizontal aragonite layers and vertical aragonite sheets of the microbialite occurs, which are considered as a product of high photosynthesis at decreasing degree of inhibition. (iii) Finally, at low supersaturation and almost lack of inhibition, syntaxial growth of aragonite crystals at lamellae surfaces leads to thin fibrous aragonite veneers. While sulfate reduction, methylotrophy, methanogenesis and ammonification play an important role in element cycling of the

mat, there is currently no evidence for a crucial role of them in CaCO_3 precipitation. Instead, photosynthesis and exopolymer degradation sufficiently explain the observed pattern and fabric of microbialite formation.

Key words: Calcification, cyanobacteria, exopolymers, microbialite, microbial mat, photosynthesis

1. Introduction

The formation of microbial carbonates, known from the Archaean to present-day, is driven by a variety of microbial processes, either affecting the ion activity product $\text{Ca}^{2+} \times \text{CO}_3^{2-}$ or kinetics of nucleation processes (for review see Riding 2000; Dupraz et al. 2009). Recent investigations focus on potential impact of anaerobic oxidation of methane or sulphate-reduction and heterotrophic activity on microbialite formation (e.g., Aloisi et al. 2002; Baumgartner et al. 2006), while e.g. photosynthetic CO_2 -assimilation has long been recognized as potentially driving microbial CaCO_3 precipitation (von Pia 1934). However, the complexity of microbial communities and the difficulty in quantifying the various effects make it demanding to elucidate few key factors that control *de facto* mineral precipitation, microbialite fabric formation and distribution. Identification of such key factors, however, is crucial to derive implications from microbialites for the reconstruction of fossil environments through Earth History.

One setting of modern microbialite formation is represented by halite lakes and hypersaline lagoons, i.e. seawater concentrated by evaporation. While the initial idea was that microbialites growth is favoured here by the lack of biofilm-grazing metazoa (Garrett 1970), lacking because of high salinities, later suggestions argue that increased calcium carbonate mineral saturations are the major prerequisite for microbialite growth (Kempe & Kazmierczak 1990). Apart from that, a high number of present-day microbialite forming settings is known, from thermal and karstwater springs to halite lakes, soda lakes, and marginal marine settings (e.g., Kempe et al. 1991; Reid & Brown 1991;

Winsborough et al. 1994; Jones & Renaut 1996; Arp et al. 1998, 2010; Laval et al. 2002; Dupraz et al. 2004; Pentecost 2005; Lim et al. 2009). In these settings, thin biofilms rather form well-laminated stromatolites, whereas thick microbial mats produce coarse-laminated to highly-porous, irregular microbialites.

In 2002, we discovered highly-porous reticulate microbialites below thick microbial mats in hypersaline lakes on the atoll of Kiritimati, Republic of Kiribati, Central Pacific. Previously, friable patchy CaCO₃ precipitates related to organomineralization have been reported from photosynthesizing thick microbial mats of brackish marine lakes, which are numerous on this atoll (Defarge et al. 1996; Trichet et al. 2001). The hypersaline lakes are filled with evaporated seawater, with no siliciclastic influx, but temporal surface recharge with meteoric freshwater. In this paper, we describe the environmental setting, prokaryotic composition and structure of the microbial mats as well as fabric and geochemistry of their microbialites. Finally, we assess the relative importance of exopolymer degradation, sulfate reduction, methanogenesis and methylotrophy, and photosynthetic CO₂ assimilation in the formation of the microbialites.

2. Location and environmental setting

The atoll of Kiritimati (formerly Christmas Island), discovered by Captain James Cook on December 24 in 1777 (Woodroffe & McLean 1998), is part of the Northern Line Islands of Republic of Kiribati (Central Pacific), located close to the Equator (1°55' N, 157°25' W) in the equatorial dry belt (Valencia 1977; Government of Kiribati 1993). The atoll is 41 km long from NW to SE and 25 km from N to S coast at the western end (**Fig. 1**). It is the largest atoll of Earth as defined by land area (ca. 360 km²; Valencia 1977; 321 km² Woodroffe & McLean 1998). The region shows a uniformly dry climate (Valencia 1977), however, affected by El Niño Southern Oscillation (ENSO), causing heavy rainfall approximately every 4 years (Falkland & Woodroffe 1997; Trichet et al. 2001; **Fig. 2**).

Numerous lakes (ca. 500; Trichet et al. 2001), with salinities ranging from nearly fresh to hypersaline (Saenger et al. 2006), occupy the inner parts of the atoll (**Fig. 1**). Most of them harbour microbial mats. The lakes are separated by a net-like system of subfossil ridges of reef carbonates (4500 to 1500

radiocarbon years BP; Woodroffe & McLean 1998). Below that, reef carbonates penetrated by drillings are of Mid-Pleistocene age or older (Woodroffe & McLean 1998). Gravity and magnetic surveys suggest that the volcanic basement is at shallow depths at the northern end of the island (Northrop 1962). There is no source of siliciclastic or volcanoclastic influx on the island.

The distinct morphology of the atoll, with a lagoon in the west, reticulate ridges with lakes in the centre and a largely dry eastern part (**Fig. 1**), reflects at least partly a drop in sealevel after a Mid-Holocene highstand (Valencia 1977, Woodroffe & McLean 1998) and possibly a northwestward tilting of the atoll (Valencia 1977). However, the channel connecting the lagoon with ocean may rather reflect a leak point (Purdy & Gischler 2005) than an opening caused by tectonic tilting. From 1957-1958 and in 1962, atmospheric nuclear tests (H-Bombs) were conducted directly above or near Kiritimati by the British military and by US army, respectively.

Recent studies focussed on carbonate-organic sediments in brackish water lakes as related to El Niño (Trichet et al. 2001), hydrochemistry (Saenger et al. 2006), the effect of salinity on the D/H ratios of lipid biomarkers (Sachse & Sachs 2008), and carbon fixation and lipid biomarkers in the microbial mats (Büring et al. 2009). The present study concentrates on four hypersaline lakes in the northern part of the atoll: Lake 2, 21, 22, and 51 (**Fig. 1**). In addition, hydrochemistry data have been obtained from further, brackish lakes, lagoonal waters, rainwater, groundwater and seawater, with locations provided in **Fig. 1**.

Figure 1. Map of the atoll of Kiritimati showing the locations investigated in this study.

Figure 2. Kiritimati rainfall data for the years 1951-2002 showing El Niño Southern Oscillation (ENSO).

3. Material and Methods

Hydrochemistry

Water samples for titration of total alkalinity were collected in Schott glass bottles, and for determination of main anions and cations in pre-cleaned PE-bottles. Samples for cation analysis were filtered in the field through 0.8 µm membrane filters (Millipore) and fixed by acidification. Samples were stored cool and dark until laboratory measurements. Temperature, electrical conductivity, pH, and redox potential of water samples were recorded *in situ* using a portable pH meter (WTW GmbH) equipped with a Schott pH-electrode calibrated against standard buffers (pH 7.010 and 10.010; HANNA instruments), and a portable conductivity meter (WTW GmbH). Dissolved oxygen was analysed titrimetrically following the Winkler method. Total alkalinity was determined by acid-base titration immediately after sampling using a hand-held titrator and 1.6 N H₂SO₄ cartridges as titrant (Hach Corporation). Main cations (Ca²⁺, Mg²⁺, Na⁺, and K⁺) and anions (Cl⁻, SO₄²⁻, and NO₃⁻) were analysed by ion chromatography with suppressed conductivity detection (Dionex Corporation). ICP-OES (Perkin Elmer) was used to determine Sr²⁺ and Ba²⁺. Dissolved phosphate and dissolved silica concentrations were measured by spectrophotometric methods (Unicam). Measured values were processed with the computer program PHREEQC (Parkhurst & Appelo 1999) in order to calculate ion activities and *PCO*₂ of the water samples as well as saturation state with respect to calcite, aragonite and gypsum. Hydrochemical model calculations have been carried out using the same program.

Microbial mat fixation, staining, embedding and sectioning

Microbial mat samples were collected using pre-cleaned sterile plastic cores and tubes. The samples were fixed with PBS (phosphate buffered saline) buffered 3.7% formaldehyde for 4-8 h, rinsed with filter-sterilized PBS-buffered sampling site water, and kept cool in the dark until. After five days of transport to the home lab, samples were either stored at 4 °C (for thin sectioning), or transferred via a graded ethanol series to 70% EtOH and frozen at -20 °C (for 16S rDNA analysis) until further processing. For labelling microbial cells, bulk samples were stained prior to embedding for 24 h in a 90% EtOH solution containing 3 µg/ml DAPI. After final dehydration in a graded ethanol series,

samples were embedded with LR White (LR White resin, medium grade; London Resin Company Ltd., Reading, UK) according to the manufacturer's instructions, cut with a saw microtome (Leica) to thickness of 70 μm , mounted on glass slides with K rapox (K mmerling Chemische Fabrik GmbH, Pirmasens), and sealed by Biomount (Electron Microscopy Sciences, Hatfield, PA) and cover slips.

Phylogenetic analysis of prokaryotes

Phylogenetic analyses of the prokaryotic communities were carried out using mat core samples, cut and subdivided in macroscopically different layers under a clean bench in the lab. DNA was extracted from 30-60 mm^3 aseptically cut material of each layer using the Qiagen DNeasy® Tissue Kit, following the manufacturer's protocol and eluted with 100 μl TE buffer. The PCR amplifications of 16S rRNA genes from the total DNA were performed with specific forward primers annealing at the 616 V binding site combined with universal 1525 R primer (**Tab. 1**) using the "SilverStar" Taq-polymerase (Eurogentec) or "Taq DNA polymerase" (Invitrogen). PCR assays that did not yield a clear amplicon were reamplified (nested PCR-approach) using the same forward primer and the universal 1492 R primer.

Cycling conditions in the PTC-200 (MG-Research) and Primus 96 (MWG-Biotech) cyclers were as follows: initial denaturation (2 min at 95°C), followed by 33 cycles of denaturation (40 s at 94°C), primer annealing (30 s + 1 s at 51°C), elongation (2 min + 2 s at 72°C) and a final 6 cycles of denaturation (40 s at 94°C) and elongation (2 min at 72°C). The PCR products purified with the EasyPure DNA Purification Kit (Biozym) were cloned into plasmid cloning vector pCR®4-TOPO®, according to the manufacturer's directions, using TOPO® TA Cloning Kit for Sequencing (Invitrogen, San Diego, California). Competent *Escherichia coli* cells, strain DH5a were used and grown on LB medium containing ampicillin. The transformant clones were selected using α -complementation and used for PCR colony screening with M13 vector specific primers. Analytical digestions with restriction enzyme Rsa I (four cutter) were performed for the characterization of different genotypes of the clones. Inserts representing different genotypes were reamplified using M13 R and T7 F primers and subsequently purified using EasyPure DNA Purification Kit (Biozym). Both strands of DNA were sequenced using the Big Dye Terminator V2.0 Cycle Sequencing Kit with a set of sequencing primers

(610RII, 609VII, 699R, T3R, T7V). Further primers used were 1492* R, 1525* R, M13 R, M13 F, and 614V. All sequencing primers are listed in **Tab. 1**. Reactions were made in 0.2 ml plastic tubes with reaction volumes 10µl using the PTC-200 (MG-Research) cycler. Sequencing products were run on an ABI 3100 automated sequencer according to the manufacturer's directions. The partial sequences, edited with Chromas, were subsequently assembled with the AlignIR Version 1.2 software (LI-COR). Sequencing the primary amplicon directly without cloning retrieved 11 unambiguous 16S-variants. These amplicons were obtained with universal primers and are considered to represent dominant microorganisms of the respective subsample. Using more selective primers, in combination with a nested PCR approach, resulted in more heterogeneous amplicons that could not be sequenced directly and had to be cloned in order to obtain homogeneous template DNA suitable for sequencing. Sequence data obtained directly from homogeneous PCR products were denoted with a number code preceded by "PCR", sequences retrieved via cloning were denoted with numbers preceded by "clone". Sequences were checked for possible chimeric origins by CHECK_CHIMERA software of the Ribosomal Database Project (Cole et al. 2003) and the Bellerophon Server (Huber et al. 2004; <http://foo.maths.uq.edu.au/~huber/bellerophon.pl>). Sequence data were submitted to GenBank under accession numbers HM480169 to HM480268, and HQ191223. Complete 16S-sequences were compared with the GenBank nucleotide data library using megablast searches (Altschul et al. 1997; <http://www.ncbi.nlm.nih.gov/blast/blast.cgi>) to find the most similar sequences publicly available. For each 16S sequence the most similar GenBank entries were downloaded and incorporated into the alignment. Alignment of the sequence data was performed manually using the MEGA version 4 (Tamura et al. 2007; <http://www.megasoftware.net/>). Distance and phylogenetic analyses were conducted using the same program. For phylogenetic reconstruction, the neighbor-joining method was employed and the reliability of the phylograms was assessed using bootstrap analyses (one thousand bootstrap replicates). Bootstrap values above 70 % were considered significant support for particular branches.

Microscopy

Laser-scanning microscopy of hardpart biofilm sections was carried out using a Zeiss LSM 510 Meta NLO attached to a Zeiss Axiovert 200 M, equipped with an Ar-laser, two HeNe-laser (Carl Zeiss MicroImaging, Jena), and a femtosecond-pulsed Titan-Saphir-Laser Chameleon XR (Coherent, Dieburg). Emission fingerprinting and linear unmixing was carried out using a 32-channel diode array (Metadetector) and software of Carl Zeiss MicroImaging, Jena.

Mineralogical analysis

The mineralogical composition of 15 microbialite and 4 mat samples was determined by X-ray diffraction analysis of whole-rock powder using a Philips instrument (control unit PW 3040, goniometer PW 3050, X-ray tube PW 3373/00, sample stage PW 1774, monochromator PW 3123/00, detector PW 3011) operating at 40 kV and 30 mA with monochromated Cu K alpha radiation (2 sec/0.02° step).

Elemental analysis

The elemental composition of 3 microbialite samples was determined by electron microprobe analysis. Carbon-coated polished thin sections of LR-White-embedded samples were used. The analyses were performed at 15 kV and 12 nA on a JEOL JXA 8900 RL electron microprobe at the Institute of Geochemistry, Göttingen. Ca, Mg, Sr, S, Fe and Mn were analyzed for 30 seconds, whereas Si, Na, and Al were analyzed for 15 seconds. Typical detection limits (1 σ count stat.) are 180 ppm for Na, 220 ppm for Ca, 90 ppm for Mg, 140 ppm for Sr, 150 ppm for Fe, 180 ppm for Mn, 140 ppm for S, 240 ppm for Si, and 140 ppm for Al.

Stable isotope analysis

Samples for carbon and oxygen stable isotope measurements have been obtained under a binocular from cutting planes (slab counterpart of thin sections) and hand specimen using a steel needle. Carbonate powders were reacted with 100% phosphoric acid (density >1.95) at 70°C using a Thermo Kiel VI carbonate preparation line connected to a Finnigan Delta plus massspectrometer. All values are

reported in per mil relative to V-PDB by assigning a $\delta^{13}\text{C}$ value of +1.95 ‰ and a $\delta^{18}\text{O}$ value of -2.20 ‰ to NBS 19. Reproducibility was checked by replicate analysis of laboratory standards and is better than ± 0.05 (1 σ). The stable isotope measurements have been carried out at the laboratory of Andreas Pack, University of Göttingen.

Table 1. Primers used in this study for amplifying and sequencing prokaryotic 16S rDNA. F at the end of a primer name indicates the forward (5'→3') direction, and R the reverse (3'→5') direction. * Asterix indicates that primer was modified for this study.

4. Results

4.1. Hydrochemistry of lake and ground waters

Selected lakes as well as marine and meteoric waters at Kiritimati have been analyzed with respect to physical and physicochemical parameters, cations, anions and nutrients. Based on that, PCO_2 and saturation with respect to CaCO_3 minerals and gypsum have been calculated (**Tab. 2**). Four types of waters can be distinguished: (1) seawater and lagoonal waters, (2) brackish lakes, (3) meso- and hypersaline lakes and their pore waters, and (4) fresh to brackish groundwaters. Ternary plots of major cations and anions (**Fig. 3**) demonstrate that all waters, except for the meteoric freshwaters, belong to Na-Cl-type, characterized by major ion ratios similar to that of seawater. For Lake 22, salinity data are available that document a decrease in salinity from 149 ‰ in 1988 to 140 ‰ in 1990 (Trichet et al. 2001), and finally 132 ‰ in 2002 (this paper), which probably reflect increasing El Nino intensity (**Fig. 2**). This trend, superimposed by intermediate dry years with increased evaporation, has also been reported by Saenger et al. (2006).

The general relation of lake waters on Kiritimati in comparison to seawater is depicted by a cross-plot of Mg^{2+} versus conservative ion Na^+ (**Fig. 4A**). This cross-plot demonstrates strict covariation of both ions, explained by evaporation of seawater, and dilution of seawater by rain water, respectively:

Lagoonal seawater is slightly concentrated by evaporation from normal seawater, with highest concentrations during low tide due to reflux from distal lagoonal parts. Brackish lake waters represent seawater diluted by meteoric waters. Hypo- and hypersaline lake waters result from evaporation from seawater, and fresh to brackish groundwater's represent a mixture of meteoric freshwater and seawater (**Fig. 4A**).

The impact of aragonite and gypsum precipitation, going along with evaporation, on seawater-derived lake waters is shown by cross-plots of Mg^{2+} versus Na^+ , and Ca^{2+} versus Na^+ , respectively (**Fig. 4A, B**). The angled arrow indicates the calculated pathway of seawater evaporation plus aragonite and gypsum precipitation. With regard to hypersaline lakes, only Lake 51 (Manulu Lagoon) closely matches this model pathway, whereas Lakes 2, 21, 22 and their pore waters show higher Ca^{2+} and higher SO_4^{2-} than predicted (**Fig. 4B, C**). The same applies to Lake 30, a mesosaline lake with microbial mats containing patchy aragonite and Mg-calcite precipitates. Hence, an increased level of inhibition of precipitation or an additional source of Ca^{2+} and SO_4^{2-} is likely for the microbialite-forming hypersaline lakes, e.g. by surface or groundwater influx. Yet, water from a crab burrow in an artificial trench at Lake 21 (**Fig. 6**) shows only a minor increase in Ca^{2+} concentration, but no increase in SO_4^{2-} (**Fig. 4B, C**). In turn, some brackish lakes (pit Banana Village, Lake 53) show a relative depletion in Ca^{2+} , but not in SO_4^{2-} (**Fig. 4B**). This coincides with high alkalinities (**Fig. 4D**) and undersaturation with respect to gypsum (**Tab. 2**). Consequently, these values likely reflect $CaCO_3$ precipitation, ammonification and sulfate reduction in nutrient-rich groundwaters in contact with these lakes (**Fig. 4D**). Contrary the clear relation between evaporation, precipitation and Ca^{2+} concentrations, there is no correlation between Na^+ concentrations and aragonite supersaturation except for seawater and lagoonal waters (**Fig. 5A**). However, a weak negative correlation of pH and salinities (Saenger et al. 2006) as well as a weak positive correlation is evident for pH and aragonite supersaturation (**Fig. 5B**), with increasing pH reflecting decreasing PCO_2 (**Tab. 2**). Nonetheless, deviations from this trend are obvious: Hypersaline lakes which contain microbialites show, at similar pH, higher aragonite supersaturation values than brackish water lakes. Again this may point to a possible influx of Ca^{2+} from subfossil carbonates via meteoric waters, and/or a high degree of inhibition of aragonite precipitation in these hypersaline lakes.

With respect to nutrients, Si, PO_4^{3-} and NH_4^+ , lakes on Kiritimati show a wide range in concentrations (**Tab. 2, Fig. 5C, D**). For comparison, seawater and lagoonal waters at Kiritimati are characterized by low Si, low PO_4^{3-} and NH_4^+ , i.e., oligotrophic. Hypersaline lakes show very low PO_4^{3-} , low NH_4^+ , but clearly increased Si relative to seawater (**Fig. 5C, D**). Their anoxic porewaters finally show high NH_4^+ and Si concentrations, at similar PO_4^{3-} . Brackish lakes have strongly varying Si, PO_4^{3-} and NH_4^+ values (**Fig. 5C, D**). Among them, an artificial pit near Banana Village with close contact to groundwaters shows extraordinarily high NH_4^+ , possibly due to the proximity to human settlements. This may also apply to Lake 54, which is close to a cementery.

Table 2. Hydrochemical data of seawater, lake, rain and ground waters of the Kiritimati atoll. Saturation index $\text{SI}_{\text{Calcite}} = \log \Omega_{\text{Calcite}} = \log (\text{ion activity product } \{\text{Ca}^{2+}\} \times \{\text{CO}_3^{2-}\} / \text{solubility product } K_{\text{calcite}})$.

Figure 3. Ternary plots of mole percentages of major anions and cations from lake, pore, ground and rain waters of Kiritimati. For comparison, several microbialite-hosting lakes from Germany, Mexico, PR China and USA are shown (Winsborough et al. 1994, Arp et al. 1998, 1999, 2001), too.

Figure 4. Relation of evaporation, dilution, and mineral precipitation on bulk water chemistry in Kiritimati lake, pore, and groundwaters. A. Cross-plot of Na^+ versus Mg^{2+} showing the effect of evaporation and dilution, respectively, on concentrations. B. Cross plot of Na^+ versus Ca^{2+} showing the effect of evaporation (dashed line) and evaporation plus aragonite and gypsum precipitation (angled arrow) on Ca^{2+} concentrations. C. Cross plot of Na^+ versus SO_4^{2-} showing the effect of evaporation (dashed line) and evaporation plus gypsum precipitation (angled arrow) on SO_4^{2-} concentrations. D. Cross plot of Na^+ versus alkalinity showing the variable effect of ammonification and sulfate reduction on the alkalinity of the different lakes.

Figure 5. Aragonite saturation index (SI_{Arag}) and nutrient conditions in Kiritimati lake, pore, and groundwaters. A. Cross plot of Na^+ versus SI_{Arag} showing no covariation. B. Cross plot of pH and

SI_{Arag} showing a weak positive correlation of both parameters. C. Cross plot of PO₄³⁻ versus Si demonstrating increased nutrient supply in pore waters and brackish lakes. D. Cross plot of pE versus NH₄⁺ showing increased ammonium concentrations in reducing, anoxic pore waters and water bodies in contact with anoxic groundwaters.

4.2. Overview on microbialite occurrences

Modern calcareous microbialites investigated in this study grow in the hypersaline and hydrologically closed lakes on Kiritimati (**Fig. 6A, B**). These are Lakes 2, 21 and 22 (**Fig. 1**), which are cut off from seawater reflux, except for potential spill-over during high sealevel. On the other hand, the hypersaline Lake 51 (Manulu Lagoon), which has a canal-like connection the marine lagoon, shows only fossil microbialite crusts at its dry shore. Also, all brackish to mesosaline lakes investigated in this study do not show lithified microbialites below the microbial mats, although the latter contain patchy friable CaCO₃ precipitates (Trichet et al. 2001).

Substrate bedrocks of the modern microbialites are, as far as visible at the shore of the different lakes, subfossil microbialite-cemented oyster beds which cover Holocene lagoonal reef debris, i.e., *Acropora* gravel with marine molluscs (**Fig. 7**). The microbialite-cemented beds ("carbonate hardpan" in Saenger et al. 2006) show polygonal tepee structures, traceable from the dry shore to peripheral parts of the lake bottom, where their ridges of the present-day microbialites reproduce the tepees below (**Fig. 7**). Towards the lake centre these tepee-forming Holocene carbonate crusts are apparently overlain by a gypsum bed, as encountered in digs in Lakes 21 and 22.

The thickness of microbialites varies between the lakes. In Lake 21, the microbialites are below the 3-5 cm thick microbial mat (**Fig. 6C, D, E**) and reach thicknesses from less than 1 cm near the lake shore (3 m off the water line at 20 cm depth) to 50 cm within the lake (ca. 20 m off the water line, at 1.5 m depth; **Fig. 7**). Intercalated are gypsum layers of 2-5 cm thickness, the most prominent approximately in the middle part of the microbialite.

In Lake 22 (**Fig. 6A, B**), calcareous microbialites are similar to that of Lake 21, but less thick and with more pronounced horizontal fabrics. The observed maximum thickness is 25 cm (ca. 20 m off the water line, at 0.5 m depth), while farther inside the lake (ca. 30 m off the water line) only 1 cm friable microbial carbonate covering a massive gypsum plate was found below the microbial mat.

In Lake 2 (**Fig. 6 F**), the microbialites are very friable and only consist of loosely cemented spherulite sands with an observed maximum thickness of 8 cm (ca. 10 m off the water line, at 05 m depth).

No present-day microbialites have been found below the microbial mats in Lake 51 (Manulu Lagoon). Instead, platy gypsum precipitates occur at the lake bottom. Nonetheless, plate-like microbialite chips are distributed upon the tepee-structure-dissected subfossil microbialite-oyster crusts of the dry shore.

Figure 6. Field images of hypersaline lakes on Kiritimati and their microbial mats, August/September 2002. A. Aerial view of Lakes 21, 22, and 51 from north. B. Lake 22 dry shore showing subfossil microbial crust with tepee structures. C. Lake 21 underwater photograph showing orange coloured microbial mats with tuft-like protuberance at approximately 1.5 m depth. D. Lake 21, white microbialite surface below 5-cm-thick microbial mat at approximately 40 cm depth (dig #2). E. Lake 21 dig #3 colour-zoned microbial mat cut in the home laboratory, displaying spherulites in its top and middle parts, and microbialite layers in its basal part. F. Lake 2 microbial mat with clear colour-zonation and white spherulitic microbialite.

Figure 7. Geological-hydrological setting of marginal parts of the hypersaline Lake 21 with its microbialites, August/September 2002.

4.3. Microbial mat structure and prokaryote community

Microbial mats of hypersaline lakes attain thicknesses between 2 and 5 cm, with greatest thickness at depths more than 1 m. Here, their orange coloured surfaces show tuft-like projections into the water column (**Fig. 6C, D**). All investigated mats, i.e., mats in Lake 2, 21, 22 and 51, show an orange top

layer, a green layer below, followed by a purple layer and a grey to brownish bottom zone (**Fig. 6E, F**). With respect to molecular biological investigations, emphasis has been placed on the identity and possible function of non-phototrophic prokaryotes, while cyanobacteria were described on basis of morphological features only. Future investigations using CARD-FISH applied to cryosections (Shiraishi et al. 2008b) are required to assign phylotypes to specific morphotypes. Based to the current data available, the distribution of prokaryotic phylotypes of the groups targeted by the primers used (i.e., exclusive *Cyanobacteria*) is shown for each layer in **Figure 9**.

Orange layer

The orange layer (0-20 mm below top) is dominated by colonies of coccoid *Cyanobacteria* with more or less vertically arranged filamentous cyanobacteria in between. Cyanobacterial morphotypes comprise *Aphanothece*, *Entophysalis*, *Leptolyngbya*, *Microcoleus*, *Spirulina*, and *Johannesbaptistia*, i.e., similar to a community described from ponds of the Rangiroa atoll (Richert et al. 2006). Rarely, empty tests of diatoms of the genus *Navicula* have been encountered at the mat top. The coccoid morphotype *Aphanothece*, together with *Leptolyngbya*, is the dominant cyanobacterium in the orange top layer. *Aphanothece* comprises ovoid cells that are 4 - 5 μm in diameter and 8 μm long. Cells are commonly in pairs due to binary fission, and group in microcolonies within a poorly layered, diffuse sheath (Fig. 8F). *Leptolyngbya* trichomes consist of cells 0.75 - 1.0 μm in diameter and 1.5 - 2.5 μm long, enclosed by a thin firm sheath (Fig. 8B). The total filament diameter is 1.5 - 2.0 μm . Empty sheath of this morphotype, probably because of their resistance against degradation, are widespread throughout the deeper mat layers. A second coccoid cyanobacterial morphotype, *Entophysalis*, is of subordinate importance in the orange top layer. *Entophysalis* is represented by colonies 20 - 100 μm in size, composed of spherical cells of 5 - 7 μm diameter. Locally, an arrangement of cells in vertical rows is evident (Fig. 8B). *Microcoleus-Spirulina*-strands of 30-150 μm diameter are conspicuous and already visible at low magnification (Fig. 8C). These strands initially consist of twisted *Microcoleus* trichomes (3.5 - 4.0 μm in diameter, with cells 4.3 - 6.6 μm long, cell walls being slightly constricted), which are increasingly associated with numerous *Spirulina* trichomes (1.5 μm cell diameter), all enclosed within a common sheath envelope. Large strands finally show abundant *Spirulina* with only

few *Microcoleus* trichomes. The surface of the common sheath envelope shows numerous attached non-phototrophic bacteria. A peculiar, though less abundant morphotype in the orange layer, is *Johannesbaptistia pellucida*. Its discoid to half-spherical cells of 8-15 μm diameter are arranged in one row within a common sheath and form slightly wavy pseudofilaments (Fig. 8D). Few pseudofilaments are scattered throughout the orange and green layer. Only between 13-19 mm below the top of the mat (i.e., deeper part of the orange layer) this morphotype is common. In general, the genus *Johannesbaptistia* is known to occur in tropical, heliothermal water bodies poor in nutrients, and in Yellowstone thermal springs (Komárek & Anagnostidis 1999). The coccoid morphotype *Chroococcus*, in the orange top layer with only scattered occurrence, shows spherical to semispherical cells of 2.0-3.5 μm diameter. Colonies of 10-20 μm diameter consist of 4-16 cells. Characteristic are successive binary fissions that result in packages of 4-8 cells, and a clear firm sheath enclosing the cell packages (Fig. 8E). A second species with 5-10 μm cell diameter was found in top parts of Lake 22 microbial mat. Thin sheathless filaments of 0.5 μm diameter, with 1.2 - 2.0 μm long cells, which occur throughout this layer and the green layer below, may represent *Chloroflexi*. Between the phototrophs, numerous coccoid, rod-shaped and filamentous bacteria are distributed (Fig. 8E, F).

16S rDNA sequences obtained from the orange layer (Tab. 3, Fig. 9, 10) demonstrate the presence of *Alphaproteobacteria*, among them representatives of the *Rhizobiales*, which comprise endophytes as well as rhizosphere bacteria (*Phyllobacterium myrsinacearum* FJ405362, *Mesorhizobium* sp. AJ2950). In addition, a close relative of *Methylobacterium populi*, i.e. a pink-pigmented aerobic, facultatively methylotrophic, methane-utilizing bacterium (Van Aken et al. 2004; Green 2006) has been detected. Furthermore, a relative of *Caulobacter* (with 97% sequence similarity to insect intestine clone D AJ459874) and one clone of the order *Sphingomonadales* were obtained. Both, *Caulobacterales* and *Sphingomonadales*, are aerobic chemoorganotrophs common in oligotrophic aquatic habitats (e.g., Staley et al. 1987; Stahl et al. 1992; Cavicchioli et al. 1999). *Betaproteobacteria* are represented by several clones of the order *Burkholderiales*, which comprises genera known as soil bacteria as well as plant symbionts or pathogens to plants and animals (Palleroni 2005). *Firmicutes* are represented by relatives of the halophilic *Pontibacillus* (PCR Kir21org 11-211103 with 97% sequence similarity to *Pontibacillus* sp. TB138) and the microaerophilic carbohydrate fermenting *Aerococcus* (clone

Kir21org aB1.22 with 99% sequence similarity to the halotolerant *Aerococcus* sp. P3-2). In addition, close relatives (clones aB1.6 and aB3.3) of *Rhodococcus erythropolis* (99% sequence similarity), an actinobacterial taxon that can metabolize aromatic compounds (e.g., Lenke et al. 1992), were detected in the orange layer.

Green layer

The green layer shows abundant colonies of the cyanobacterial morphotype *Aphanothece* which are largely in the state of dying and decay. Instead, *Chroococcus* colonies ("large morphotype") are common (**Fig. 8E**), associated with few *Johannesbaptistia* pseudofilaments. 3.5 to 4- μ m-sized coccoid cyanobacterial cells with individual 2- μ m-thick sheaths (small *Chroococcus* morphotype) are distributed throughout the layer, while filamentous *Cyanobacteria* are rare and largely restricted to empty sheaths of *Leptolyngbya*. In general, this layer shows a successive degradation of the primary exopolymer fabric, with increasing horizontal structure and spatial enrichment of carbonate particles (Fig. 8A). Numerous coccoid, rod-shaped and filamentous non-phototrophic bacteria occur throughout the layer.

16S rDNA sequences obtained from the green layer (Tab. 3, Fig. 9, 10) show a dominance of alpha- and betaproteobacterial taxa with respect to the non-cyanobacterial prokaryotic community. Among the *Alphaproteobacteria*, members of the *Sphingomonadales* are now most common, while members of the *Rhizobiales* and *Caulobacterales* remain present. The *Betaproteobacteria* are, similar to the orange top layer, largely represented by members of the *Burkholderiales*, with close relatives from soils. One betaproteobacterial partial clone sequence (clone Kir21grn bB8.2*) was found to be 96% identical to the uncultured bacterium AY053477, which was associated with marine gas hydrates (Gulf of Mexico; Lanoil et al. 2001). Two clones of *Gammaproteobacteria* have been detected, with close relatives to uncultivated bacteria from seafloor hydrothermal vent and settings of anaerobic ammonium oxidation, respectively. Also, *Bacterioidetes*, yet without evidence in the orange top layer, occur in the green layer. Their nearest relatives are known from microbial mats of hypersaline and sulfidic environments, respectively. Again, one clone with 99% sequence similarity to *Rhodococcus erythropolis* was retrieved. Conspicuous is the presence of representatives of the candidate division

TM6, detected by several clones. Similar to the orange top layer, sequences obtained from PCR products using universal primers demonstrate the abundance of halophilic *Firmicutes* of the genus *Pontibacillus*. One clone (clone 21gfCA.1*) could be assigned to the phylum *Crenarchaeota* and showed 99% sequence similarity with an uncultured crenarchaeote from a hypersaline pond microbial mat of Guerrero Negro, Baja California (Robertson et al. 2009).

Purple layer

The purple layer is characterized by abundant empty spheroidal cell envelopes of 10 μm diameter and with binary fission (Fig. 8G). They likely present sheaths of dead cyanobacterial cells of the small *Chroococcus* variety mentioned from the green layer. Cell groups of the large *Chroococcus* variety are still common. Due to their autofluorescence characteristics, spherical cells of 2 μm diameter, commonly in groups of 2-8 cells, are likely purple bacteria (Fig. 8G). Numerous empty cyanobacterial sheaths, predominantly *Leptolyngbya*, occur besides of abundant rod-shaped bacterial cells of 1.0-1.5 μm size.

Only few 16S rDNA sequences are available from this layer (Tab. 3, Fig. 9, 11). Sequences obtained from PCR products using universal primers (PCR Kir51pur 18-211103; Kir21pur 7-211103) indicate the abundant occurrence of halophilic *Firmicutes* of the genus *Pontibacillus* in this layer from both lakes, 51 and 21. In addition, one clone (Kir21pur d37), with 99% sequence similarity to clone ET5_1G3 from a microbial mat of Guerrero Negro, Baja California (Orphan et al. 2008), demonstrates the presence of *Thermoplasmatales*.

Grey and brown layers

The grey bottom zone of the mats and brownish flocculent EPS of microbialite pore spaces exhibit numerous coccoid and rod-shaped non-phototrophic bacterial cells 1-2 μm in size. Occasionally, sarcina-like cell aggregates were observed (**Fig. 8K**).

For the grey layer, most sequences were obtained for the *Alphaproteobacteria* and *Firmicutes* (Tab. 3, Fig. 9, 11). Among the *Alphaproteobacteria*, one clone could be assigned to the *Rhodobacterales*, a group which comprises the non-sulphur purple bacteria. Most alphaproteobacterial clones of this layer,

however, are members of the *Rhizobiales*, with close relatives described from a hypersaline microbial mat of Puerto Rico (Isenbarger et al. 2008). One clone showed 99% sequence similarity to *Methylobacterium fujisawaense* DSM5686 AY169421.1. This species grows on methanol and thiosulfate in nutrient-limited mixotrophic conditions (Anandham et al. 2009). *Betaproteobacteria* are represented by a relative of *Janthinobacterium lividum*, known from soil and water samples. This taxon is known to produce chitinases (Gleave et al. 1995) (note insect remain in this mat part shown in **Fig. 8I**). In addition, single clones of the *Gammaproteobacteria*, *Acidobacteria* and *Chloroflexi* (green non-sulfur bacteria) were detected. Several clones as well as a sequence obtained directly from PCR products indicate the abundance of *Firmicutes* of the *Pontibacillus-Halobacillus* clade. Also, *Halanaerobiales* and *Clostridiales* are present, as proven by single clones. The latter order is represented by a relative of the strictly anaerobic *Desulfonispora thiosulfatigenes* DSM 11270 (91% sequence similarity), which is capable of desulfonation as well as producing acetate, ammonia and thiosulfate (Denger et al. 1999). Several clones could be assigned to the candidate divisions TM6 and KSB1, with closest relatives known from other hypersaline microbial mats (Isenbarger et al. 2008), sulfide-containing springs (e.g., AB425065; Horath et al., unpublished) or hydrocarbon-containing sediments (Winderl et al. 2009). Furthermore, clones with next relatives of uncertain phylogenetic position (Knittel et al. 2003) or provisionally arranged as "hypersaline group II (HS-II)" (Lloyd et al. 2006) were found. All of them are described from saline to hypersaline methane seepage sites. *Planctomycetes*, absent from the higher mats parts in Kiritimati lakes 21 and 51, occur in the grey layer, again with close relatives from hypersaline or methane-bearing settings, respectively. The same applies to the two *Crenarchaeota* clones detected, with next relatives from Guerrero Negro hypersaline microbial mat (Robertson et al. 2009) and anaerobic mud of a Mediterranean mud volcano (FJ649533; Kormas et al., unpublished). Microbial methane production is finally indicated by a *Euryarchaeota* sequence obtained directly from PCR product of this layer, with 97% sequence similarity to the methylotrophic *Methanohalophilus mahii* from Great Salt Lake anaerobic sediments (Paterek & Smith 1988) and 98% sequence similarity to *Methanohalophilus euhalobius* X98192 from saline subsurface waters of a Russian oil field (Davidova et al. 1997).

16S rDNA sequences obtained from the brown flocculent microbial aggregates at the top of Lake 21 microbialites demonstrate the presence of *Alphaproteobacteria*, among them members of the *Rhizobiales* and *Caulobacteriales* (Tab. 3, Fig. 9, 11). Again, one clone with 99% sequence similarity to *Methylobacterium fujisawaense* DSM5686 was retrieved. *Betaproteobacteria* comprise a member of the *Burkholderiales* with a distant relative from a soil. Two *Gammaproteobacteria* clones are closely affiliated with marine *Pseudomonas* stains. *Firmicutes* are again represented by members of the *Halobacillus-Pontibacillus* group, two of them with close relatives from Cabo Rojo hypersaline microbial mat. Also, one clone of the *Halanaerobiales*, which are halophilic anaerobes with a fermentative or homoacetogenic metabolism, has been detected. Contrary to other layers of the Kiritimati lake 21 and 51 microbial mats, *Deltaproteobacteria* could be detected, with next relative from a Pacific Eel-River-Basin methane seep (Orphan et al. 2001) and a hypersaline microbial mat of Puerto Rico (Isenbarger et al. 2008). One clone is distantly related to *Desulfococcus multivorans* DSM 2059, a sulfate-reducing bacterium which is capable of using aromatic compounds for growth and energy generation (Widdel 1980; Peters et al. 2004). One clone assigned to the candidate division OP8 and three clones assigned to the *Chloroflexi* were found, all of them closely related (97-99% sequence similarity) to clones retrieved from a hypersaline microbial mat of Puerto Rico (Isenbarger et al. 2008). This also applies to one *Planctomycetes* clone, while a second clone of this phylum is affiliated (94% sequence similarity) with a representative from a mid-ocean-ridge environment (Huber et al. 2006). Finally, two clones of *Archaea* have been retrieved from the brown flocculent microbial aggregates. One *Crenarchaeote* closely related (99% sequence similarity) to a clone from a Guerrero Negro hypersaline microbial mat, and one clone affiliated (94% sequence similarity) with the methanogenic Euryarchaeote *Methanohalophilus oregonensis* DSM 5435. Similar to the *Methanohalophilus* strains mentioned from the grey layer, this stain grows on methyl compounds, but not on H₂ and CO₂, formate, or acetate, an observation that applies to methanogens in other hypersaline, sulfate-containing anoxic environments (Liu et al. 1990).

Table 3. Operational taxonomic units (OTUs) retrieved from Kiritimati microbial mats and their nearest relatives with percentage identity to first match through BLASTn.

Figure 8: Mat structure and prokaryote communities.

- A. Vertical section through microbial mat of Lake 21, dig 3. Left column: plain view to show colour zonation. Middle column: microbial mat section in transmitted light view with crossed polarizers to show mineral components (microcrystalline aragonite, spherulites). Right column: same view under epifluorescence (excitation 365 nm, emission 397-700 nm) to show general distribution of microbial cells stained by DAPI.
- B. Mat top with *Entophysalis*, *Aphanothece* and thin filamentous cyanobacteria (*Leptolyngbya*). Top of orange layer. LSM micrograph (excitation 488, 543, 633 nm / emission 500-530, 565-615, 640-700 nm, projection of 21 planes at 1 μm z distance).
- C. Consortium of *Microcoleus* (here a single trichome) and *Spirulina*, surrounded by empty *Leptolyngbya* sheaths. Middle part of orange layer. LSM micrograph (excitation 488 nm, 543 nm, 633 nm / emission 500-530, 565-615, 640-700 nm, projection of 21 planes at 1 μm z distance).
- D. *Johannesbaptistia* between *Aphanothece* colonies and thin filamentous photosynthetic bacteria. Deeper part of orange layer, 13mm below top of microbial mat. LSM micrograph (excitation 488, 543, 633 nm / emission 500-530, 565-615, 640-700 nm, projection of 11 planes at 1 μm z distance).
- E. *Chroococcus* colonies and numerous small coccoid and filamentous cyanobacteria in middle part of green layer. Note horizontal structure of exopolymer matrix. LSM micrograph (excitation 488, 543, 633 nm / emission 500-530, 565-615, 640-700 nm, projection of 15 planes at 1 μm z distance).
- F. *Aphanothece* colonies associated with filamentous and rod-shaped non-phototrophic bacteria. Upper left corner shows margin of large aragonite spherulite. Deeper part of orange layer, 16 mm below top of microbial mat. LSM micrograph, overlay of epifluorescence (excitation 488, 543, 633 nm / emission 500-530, 565-615, 640-700 nm, projection of 11 planes at 0.5 μm z distance) and X Nicols.
- G. Purple bacteria and dead empty cells of coccoid cyanobacteria of the purple layer. LSM micrograph (excitation 488 nm, emission 490-700 nm, spectral detection) after linear unmixing. Emission maximum 550 nm shown in green, 590 nm shown in red.

- H. Oblique band of aragonite precipitates between purple bacteria, cyanobacteria and non-phototrophs. Purple layer, 28 mm below top of microbial mat. LSM micrograph, overlay of epifluorescence (excitation 488, 543, 633 nm / emission 500-530, 565-615, 640-700 nm) and X Nicols.
- I. Overview of the basal anaerobic mat part with empty cyanobacterial sheaths, numerous bacterial cells and tube-shaped insect remains. Grey-brownish basal layer of microbial mat. 2P-LSM micrograph (excitation 720 nm / emission 435-485 nm). DAPI stained.
- K. Sarcina-like prokaryote colony from brownish basal layer of microbial mat. 2P-LSM micrograph (excitation 720 nm / emission 435-485 nm). DAPI stained.

Figure 9. Distribution of prokaryotic phylotypes exclusive *Cyanobacteria* (full and partial 16S rDNA sequences) within orange, green, purple, grey and brown layers from the microbial mat of Lake 21.

Figure 10. Phylogenetic tree of sequences obtained from orange and green microbial mat parts, Kiritimati Lake 21 and 51, and their cultured and uncultured relatives with associated GenBank accession numbers. Bootstrap support values (percent; 1000 replicates; only values >70% shown) are indicated at the bases of branches. The scale bar represents 5% sequence divergence.

Figure 11. Phylogenetic tree of sequences obtained from purple, grey and brown microbial mat parts, Kiritimati Lake 21 and 51, and their cultured and uncultured relatives with associated GenBank accession numbers. Bootstrap support values (percent; 1000 replicates; only values >70% shown) are indicated at the bases of branches. The scale bar represents 5% sequence divergence.

4.3. Hydrochemical gradients across microbial mats

Physicochemical gradients detected by standard field electrodes at Lake 21 are shown in **Fig. 12**. Only data for daylight conditions available.

Conductivity measurements document a decline in salinity from the water column through the mat to pore water. Temperature reaches a maximum within photosynthetic mat parts, due to light adsorption. The pH increases from water column (8.27) at the orange top layer of the mat to a maximum value of 8.90. Within the mat, a decline to 8.60 (green layer) and finally 7.60 (grey mat basis) is observed, while in the pore water near-neutral pH was measured (7.16). Similar to pH, pE (negative log of the electron activity) increases from water column (+2.84) to a maximum value of in the orange top layer (+3.25) of the mat, then declines to +1.69 in deeper mat parts. Negative values were obtained from the mat basis (-2.10) and the pore water below the mat (-2.62).

Data of cation and anion concentrations are only available from the water column and from the pore water in the microbialite below the mats (**Tab. 2**). Based on these data, aragonite saturation is very high in the water column, whereas in pore water shows only saturation to slight supersaturation (**Fig. 12**). Alkalinity is the same above and below the mats. Ca^{2+} concentration is lower in the pore water, which, however, reflects decreased salinities (**Fig.12**). For Lake 22, pore water is much lower in Ca^{2+} if compared to the water column, but fits well to the calculated pathway of evaporation and mineral precipitation (**Fig. 4**). Low SI_{Arag} values of the pore water below the mats therefore largely reflect a high PCO_2 and hence decrease pH (**Fig. 12**). This coincides with high ammonium concentration, increased phosphate and dissolved iron (**Tab. 2**).

Figure 12. Physicochemical and hydrochemical gradients across the microbial mat in Lake 21, between dig #2 and #3, under daylight condition (04.09.2002).

4.4. Fabric and composition of microbial carbonate

Initial precipitates

Initial mineral precipitates within the microbial mats comprise three different types: (i) spherulites, (ii) streaks of aragonite needles, and (iii) gypsum crystals.

(i) Spherulites develop from initial microcrystalline (<1 μm) aggregates, with up to 50 μm in size. XRD analysis and high Sr concentrations detected by EPMA indicate an aragonite mineralogy. These patchy small aggregates already occur 0.75 mm below top of mat, and serve as nuclei for radial-fibrous veneers by aragonite needles which finally result in large spherulites 1-2 mm in size. Well developed spherulites are observed in lower half of the orange layer (e.g. 15 mm below top to the mat; **Fig. 8A**), and accumulate in the green layer by condensation of the exopolymer mat matrix.

(ii) Streaks of aragonite needles form in crevice-like zones of the exopolymer framework of the mat. These aragonite needle streaks occur first within basal parts of the green mat layer and, more intensively developed, within the purple layer of the mat (**Fig. 8A, H**). XRD analysis and high Sr concentrations detected by EPMA indicate an aragonite mineralogy for these 2-3 μm wide and 10-20 μm long needles. In addition, isometric CaCO_3 crystals less than 1 μm in size occur. Within larger aggregates, the crystals become pseudohexagonal and up to 10 μm size.

(iii) Scattered gypsum crystals occur within the exopolymer matrix through the microbial mat. First monocline crystals and twins of 15 x 50 μm size are visible already near the top of the mats. XRD analysis of freeze-dried mat samples (orange, green and grey layers) indicated gypsum and halite besides of aragonite. In addition, traces of bischofite have been detected in the grey mat basis of Lake 51.

Microbialite

The resulting microbialite, as observed below mats containing the initial precipitates described above, is characterized by a reticulate framework composed of three structural elements (**Fig. 13A, B, C**): (i) Vertical, jagged carbonate sheets and threads 0.25 - 1 mm thick with comb-like arrangement, forming 1-4 cm high layers, (ii) subhorizontal irregular, porous-friable carbonate layers of approximately 3-6 mm thickness, and (iii) gypsum crystal layers up to 5 cm thickness. The "reticulate microbialite" in Kiritmati lakes therefore differs from other microbial carbonates denominated by the same term (e.g., Pratt 1982; Kahle, 1994; Parcell 2002), but composed of clotted micrite or microbial peloids.

(i) Vertical aragonite sheets commonly show a microspar-like central zone pervaded by microcrystalline stripes (**Fig. 13C, D**). These central parts are composed of interlocking, 4 - 30 μm

sized aragonite crystals with pseudo-hexagonal habitus and dark organic inclusions (**Fig. 13D**). The central zone is enclosed by a microcrystalline marginal zone. Finally aragonite botryoids grade into fibrous veneers, which form the last phase (**Fig. 13D**).

(ii) Subhorizontal, friable layers consist of interlocking aragonite crystals, too. The layers commonly exhibit dark-brown to black dots in central layer parts, which turned out in microscopy as fossilized colonies of coccoid cyanobacteria (*Gloeocapsa* morphotype; **Fig. 13E**). In top view, subhorizontal layers of Lake 22 commonly show bubble-like voids. Associated with the subhorizontal layers are aragonitic spherulites of 100 - 500 μm diameter occur. Much larger are spherulites in Lake 2 microbial mats, which attain up to 2 mm in diameter (**Fig. 14**). They form friable carbonate sand attached to the subhorizontal layers, but occur scattered throughout the mat and enclosed in microbialite sheets as well. In one of the subhorizontal, dense layer of aragonite in Lake 2, parallel to fan-like arranged erect cyanobacterial filament traces (4-6 μm diameter, dark-brownish envelope, internally aragonitic) have been observed. Here, aragonite is composed of 4-20 μm large interlocking crystals, i.e., microcrystalline to microsparitic. Locally, fibrous smooth aragonite veneers line closed voids, and thin fibrous aragonite needles grow on spherulites and irregular laminae surfaces.

(iii) Restricted to a few horizons, e.g. 30 cm below microbialite top in digs #3 and #4, idiomorphic gypsum crystals up to 5 mm in size form horizontal levels (**Fig. 13F**). Starting with scattered aggregates attached to microbialite sheets, these crystals fuse to coalescent layers 2 cm thick (**Fig. 13A**). Also, the solid substrate below the microbialite is formed by coarse crystalline gypsum.

XRD analysis and EPMA measurements demonstrate that microbialites are composed of aragonite (**Fig. 14**). Sr concentrations in aragonitic microbialites, spherulites and fibrous aragonite cements are high, with aragonite of Lake 2 having comparatively low values (**Fig. 15**).

With respect to Mg in the aragonite, concentrations vary between 150 and 1500 ppm, with one exception of 2100 ppm. No systematic relations, e.g. between central parts of layers and fibrous veneers, were recognized. Mg-calcite is restricted to small patches and seams in microbialites cementing aragonitic spherulites of Lake 2, and miliolid foraminiferal tests in pore spaces of the microbialites in Lake 2 and 21 (**Fig. 14**). Fe and Mn concentrations are at or below detection limits. Iron sulfides have not been detected, neither by EMPA nor XRD analysis.

Figure 13. Fabric and composition of microbialites. A. Specimen of a reticulate microbialite from Lake 21, dig #3 / 3a. Note white gypsum crystals at bottom of sample. B. Same specimen in top view. C. Thin section of vertical aragonite sheets showing a microsparitic aragonite central zone, a microcrystalline marginal zone, and a fibrous aragonite veneers. Biofilm veneers (brownish flocculent aggregates) occur only in top parts of the microbialite. X Nicols. Insert: overlay of X Nicols view and fluorescence micrograph; excitation 400-440 nm; emission >570 nm. Lake 21, sample dig 5 / 5a. D. Detail of vertical sheet of microbialite, with fibrous aragonite veneer. Insert: Microspar-sized pseudo-hexagonal aragonite in central parts of the sheet. X Nicols. Lake 21 dig 3 / 3a. E. Horizontal layer of aragonite, with remains of coccoid cyanobacteria (insert). Plane polarized light. Lake 21 dig 3 / 3a. F. Gypsum crystals growing on aragonitic reticulate microbialite of Lake 21, dig 3 / 3a. Plane polarized light.

Figure 14. Top: Back-scatter electron micrograph of a spherulite-rich microbialite layer of Lake 2, dig #2, with aragonitic components appearing white, and Mg-containing calcium carbonate appearing darker. Outline of spherulites is indicated by white dashed lines. Note miliolid foraminiferal tests in pore space of the microbialite. Bottom: Electron microprobe traverse of Ca, Mg, Sr, Na and S demonstrating an aragonitic composition of the microbialite with only traces of Mg-calcite (spots 41 and 43).

Figure 15. Cross-plot of Mg and Sr concentrations in Lake 2 and 21 microbialites, measured by electron microprobe.

4.5. Stable carbon and oxygen isotopes

Stable carbon and oxygen isotopes have been analysed from lacustrine and lagoonal microbialites, including Recent as well as subfossil to Holocene precipitates. For comparative purposes, Recent as well as Holocene-subfossil skeletal carbonates have been analysed, too (**Tab. 4, Fig. 16**).

For the marine and marine-lagoonal skeletal carbonates, i.e., Holocene reef debris of a drill core at Decca (**Fig. 1**), subfossil shells and corals from vicinity of lakes, and Recent agglutinated oncoids from the lagoon at London (**Fig. 1**), values range from $-2.6\text{‰ } \delta^{13}\text{C}$ and $-6.2\text{‰ } \delta^{18}\text{O}$ to $+3.7\text{‰ } \delta^{13}\text{C}$ and $+1.0\text{‰ } \delta^{18}\text{O}$. A clear covariation of $\delta^{13}\text{C}$ and $\delta^{18}\text{O}$ with $r = 0.94$ is evident for these carbonates (**Fig. 16A**). In contrast to this, subfossil stromatolitic cements deviate from this trend by increased $\delta^{13}\text{C}$. Here, no covariation of stable carbon and oxygen isotope values is evident. Likewise, all Recent microbialitic carbonates of Lake 2, 21 and 22 are significantly enriched in ^{13}C , if compared to the marine-lagoonal skeletal carbonates (**Fig. 16A**).

Within the microbialite-hosting hypersaline lakes distinct variations in $\delta^{13}\text{C}$ at similar $\delta^{18}\text{O}$ are evident (**Fig. 16B**): Most positive values were obtained from spherulites ($+5.1$ to $+7.1\text{‰ } \delta^{13}\text{C}$) and a horizontal layer with cyanobacterial filament traces ($+6.0\text{‰ } \delta^{13}\text{C}$). In contrast, vertical sheets and horizontal layers range from values similar to that of the cyanobacterial layer in Lake 2 ($+6.3\text{‰ } \delta^{13}\text{C}$) to significantly less ^{13}C enriched ratios ($+2.5\text{‰ } \delta^{13}\text{C}$) (**Fig. 16B**).

Table 4. Stable carbon and oxygen isotopes of skeletal and microbial carbonates of Kiritimati.

Figure 16. Stable carbon and oxygen isotope values of Recent and Holocene-subfossil carbonates of Kiritimati. **A.** Cross-plot of $\delta^{13}\text{C}$ versus $\delta^{18}\text{O}$ of Holocene to Recent skeletal carbonates and microbialites. **B.** Variations of $\delta^{13}\text{C}$ and $\delta^{18}\text{O}$ of microbialites components within the hypersaline Lakes 2, 21, and 22.

5. Interpretation: Habitat, microorganisms and microbialite formation

Microbialite formation in the investigated Lakes 2, 21, and 22 currently takes place, as indicated by delicate needles of aragonite within the exopolymer matrix of their microbial mats. The mode of precipitation, however, in this actively growing microbialite system seems to be peculiar. Despite of high aragonite supersaturation in the water column and high photosynthetic activity, only minor

CaCO₃ precipitates are observed in the top parts of the microbial mat of hypersaline lakes on Kiritimati. Instead, CaCO₃ precipitates occur more excessively in lower mat parts at the transition to the anoxic zone. This observation leads to the hypothesis that exopolymer degradation and breakdown of inhibition may play a crucial role in the formation of these microbialites characterized by an enigmatic reticulate fabric. Indeed, a crucial role of exopolymers in calcium carbonate precipitation in these mats has previously been proposed by Défarge et al. (1996).

From hydrochemical point of view, the habitat of the microbialite-forming mats generally can be described as evaporated seawater. These hypersaline lake waters are highly supersaturated with respect to aragonite ($SI_{Arag} = 1.0$ to 1.3), and no significant differences in aragonite supersaturation between the microbialite-containing lakes 2, 21, 22 and the microbialite-free lake 51 (Manulu Lagoon) are obvious (**Tab. 2, Fig. 5A, B**). However, microbialite-forming lakes 2, 21, and 22 have higher Ca²⁺ than expected by simple evaporation and aragonite plus gypsum precipitation pathway from marine waters, while Lake 51 (Manulu Lagoon) fits to the pathway (**Fig. 4B**). Hence, an additional surface or groundwater influx of Ca²⁺ dissolved from Holocene carbonates to the microbialite-containing lakes 2, 21 and 22 is suggested. With respect to nutrients, the aerobic lake water column is low in NH₄⁺ and PO₄³⁻, while the anoxic pore waters below the mats show high NH₄⁺ at only slightly increased PO₄³⁻ concentrations.

The prokaryotic community certainly reflects these habitat conditions (**Tab. 3**), although a definitive proof of functional relationships cannot be made on basis of 16S rDNA analysis. Apart from the *Cyanobacteria*, which are the major primary producers, a high number of clones of other phototrophs (purple non-sulphur bacteria, *Chloroflexi*) and non-phototrophs retrieved from the Kiritimati microbial mats find their closest, commonly halotolerant, relatives in other microbial mats of hypersaline settings, particularly of the lagoon at Cabo Rojo, Puerto Rico (Isenbarger et al. 2008) and Guerrero Negro (Orphan et al. 2008; Robertson et al. 2009).

Also, phototrophic mat parts contain aerobic chemoorganotrophs, some of them with preference to oligotrophic habitats (*Caulobacterales* and *Sphingomonadales*). Finally, the genera *Burkholderia* and *Ralstonia* (both aerobic taxa which include animal and plant pathogens but also plant symbionts) as

well as soil-inhabiting bacteria point to a potential surface (plant detritus) or subsurface influx (groundwaters) from terrestrial areas. Surface influx of organic material may also be indicated by chitinase-producing phylotypes (*Janthinobacterium lividum*; Gleave et al. 1995), which is in accordance with the presence of insect remains within the mats (Fig. 8I).

Strikingly, a number of clones from the investigated microbial mats show closest relatives to microorganisms either involved in methane production (i.e., methanogenic *Archaea*) or consumption of methane or methyl compounds (e.g., *Methylobacterium populi*; Van Aken et al. 2004) or hydrocarbons (e.g., certain taxa of candidate phylum TM6; Winderl et al. 2009). Specifically, close relatives come from methanotrophic communities of seep brine pools (Hypersaline group II; Lloyd et al. 2006), Mediterranean mud volcanoes or methane seeps off the coast of North America (Lanoil et al. 2001; Orphan et al. 2001). Methanogens, represented by the genus *Methanohalophilus*, appear to be one of the dominant organisms in anaerobic mat parts. All this points to a significant role of methane and methyl components in the carbon cycle of the microbial mats.

In addition, aerobic as well as anaerobic mat parts contain representatives that potentially metabolize aromatic compounds (e.g., benzene; by *Rhodococcus erythropolis*; e.g. Fahy et al. 2008). Most likely, these organisms metabolize other organic compounds naturally occurring within the mats, but a possible anthropogenic contamination by fuel or coal tar from the former military use of the atoll cannot be excluded.

The presence of sulphate-reducing bacteria (SRB) appears to be more difficult to assess. Specific biomarkers (C₁₇ PLFAs) substantiate the presence of oxygen-tolerant sulphate-reducers in the top layer of the mats on Kiritimati (Büring et al. 2009). Nonetheless, the available clone sequence data from Kiritimati indicate *Deltaproteobacteria* only for the grey and brown-flocculent anoxic mat parts, where H₂S indeed is present although iron sulfide precipitation lacks due to low availability of iron. In the green layer, our study reveals instead representatives of the candidate division TM6, which is phylogenetically affiliated with the *Deltaproteobacteria*. In any case, experiments with ³⁵S-labeled sulfate as well as fluorescence *in situ* hybridizations indicate the presence and activity of O₂-tolerant SRB in aerobic microbial mats parts of similar habitats (Guerrero Negro; Canfield & Des Marais 1991; Risatti et al., 1994; Minz et al., 1999).

Physicochemical and hydrochemical gradients across the Kiritimati microbial mats, although available only for daylight conditions, demonstrate a high impact of oxygenic photosynthesis in upper mat parts (**Fig. 12**), a process that potentially drives CaCO_3 precipitation (Bissett et al. 2008; Shiraishi et al. 2008a). At the mat top, a pH maximum of 8.90 in combination with a pE maximum of +3.25 was observed, both values significantly higher than in the water column (pH 8.3; pE +2.84). Heterotrophic activity and oxygen consumption then successively decrease pH to near-neutral and pE to very negative values in the pore waters below the mat (**Fig. 12**).

However, detailed microscopy of thin sections shows that oxygenic photosynthetic upper mat parts contain only minor amounts of aragonite precipitates. Specifically, these are aragonite clots which initiate spherulite growth (**Fig. 8A**). These spherulites then become concentrated in the green and purple layer coincident with a decrease in cyanobacterial cells and transition from a homogeneously structured to a layered, compacted exopolymer matrix with crevice-like zones (**Fig. 8A, H**). The actual microbialite, with its horizontal layers and vertical sheets, apparently initiates exactly in these crevice-like zones. Here, in the green and purple layer of the microbial mat, pH is around 7.6 (at daylight conditions) and, hence, aragonite supersaturation with intermediate values is expected. Because of that, no exorbitant strong photosynthesis effect, but the degradation of nucleation-inhibiting exopolymers could be the driving mechanism in precipitation.

The resulting microbialite, with its fabric displaying the crevice-like weakness-zones of the exopolymer mat framework, is - with few exceptions - composed of aragonite microspar with thread-like microcrystalline stripes, i.e. is devoid of calcified cyanobacteria or other "calcimicrobe" fossils. Exceptions are conspicuous grey to black horizontal layers with coccoid cyanobacterial remains from Lake 21 and 22 (**Fig. 13E**), and one layer with erect cyanobacterial filament traces from Lake 2. These exceptions indicate that a minor part of the horizontal layers were already formed within cyanobacteria-dominated mats parts, i.e., green or even the orange mat layer, and that aragonite precipitation is not linked to a specific redox zone.

Fibrous aragonite veneers of the microbialite layers and sheets were only found in the microbialite parts below the microbial mat. Here, the carbonates show locally thin, patchy biofilms, but appear to be successively free of a continuous exopolymer cover. Instead, microbes are concentrated in

flocculent aggregates within pore spaces. Indeed, gypsum locally nucleates directly upon the carbonate framework. Therefore, a lack of exopolymer films at low but existing supersaturation is considered to permit slow overgrowth of existing carbonate crystals to form fibrous veneers on the microbialite framework.

Stable carbon and oxygen isotope values of microbialites in comparison with marine values, support the interpretation that, after a simultaneous enrichment of ^{18}O and ^{13}C in the lake water by evaporation (indicated by covariation), high photosynthesis and possibly loss of CH_4 to the water column causes very positive $\delta^{13}\text{C}$ values in the microbial carbonates (**Fig. 16**). A high depletion of ^{12}C in the organic sedimentary carbon of Kiritimati Lake 30 mats was already noted by Trichet et al. (2001) and was explained by them by a high bioproductivity. Most positive values have been obtained for spherulites and a layer with cyanobacterial filament traces, which are forming in the oxygenic mat parts as the first precipitates. Vertical sheets and horizontal layers, both starting to form in the lowermost green layer and purple layer show similar to significantly less positive $\delta^{13}\text{C}$ values, thus are consistent with dissolve inorganic carbon derived from degradation of organics combined with moderate photosynthesis. There is no indication of carbonate precipitation driven by methane consumption. Consequently, on basis of the available information, the following explanation is suggested for the formation of the reticulate microbialites in Kiritimati lakes (**Fig. 17**):

(1) In the orange layer, intensive photosynthesis causes high pH and consequently high supersaturation with respect to aragonite. However, precipitation is efficiently inhibited by pristine exopolymers of the mat layer. At few spots where inhibition is overcome, nucleation and radial aragonite crystal growth starts. Hence, these spherulites are a product of an extraordinary high photosynthesis effect simultaneous to an efficient inhibitory effect by exopolymers.

(2) In deeper parts of the green, and in the purple layer, increasing decarboxylation and hydrolysis of exopolymers cause successive break-down of inhibition. While supersaturation with respect to aragonite is decreased but still high, aragonite crystal nucleation takes place along crevice-like zones of partly degraded exopolymers. Sheet-like aragonite structures with fringed edges form. Hence,

reticulate microbialite layers and sheets are a product of high photosynthesis at decreasing inhibition of exopolymers.

(3) Within anoxic porewater below mat, inhibition of aragonite precipitation is almost absent, however, at low supersaturation to saturation. Consequently, slow, syntaxial growth of aragonite crystals at lamellae surfaces occurs. Hence, fibrous aragonite veneers of the microbialite framework are a product of low aragonite supersaturation at almost absence of inhibition.

Figure 17. Model of microbialite formation in hypersaline lakes on Kiritimati.

6. Discussion: autotrophic vs heterotrophic processes in microbialite formation

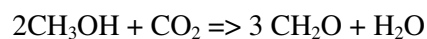
The microbialites of hypersaline lakes on Kiritimati excellently exemplify the common difficulties in identifying a specific microbial process as crucial in microbialite formation. While degradation of inhibiting exopolymers within a photosynthesis-dominated microbial system is favoured as explanation for CaCO₃ precipitation and microbialite fabric formation in this paper, a number of other processes with potential effect on carbonate equilibrium and nucleation operate at the same time. Specifically these are, based on the data available, (i) anoxygenic photosynthesis, (ii) sulfate-reduction, (iii) ammonification, (iv) methanogenesis and methylotrophy. A further question is, why microbialites form in the hypersaline Lakes 2, 21 and 22, but not in the hypersaline Lake 51.

(i) Anoxygenic photosynthetic bacteria (green and purple bacteria) potentially rise the Ca²⁺ x CO₃²⁻ ion activity product by their assimilation of carbon dioxide:



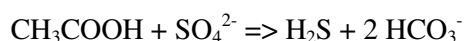
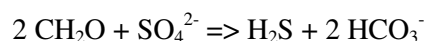
However, commonly sulfide oxidation further proceeds via elemental sulfur to sulfate, then causing acidification. Moreover, purple non-sulfur bacteria (*Rhodospseudomonas palustris*) have been shown in laboratory experiments to induce CaCO₃ precipitation in solutions already supersaturated with respect

to CaCO₃ minerals (Bosak et al. 2007). Purple non-sulfur bacteria have been shown to be metabolically versatile (Sasikala & Ramana 1998; Larimer et al. 2003), and some of them grow e.g. on methanol (Douthit & Pfennig 1976):



Indeed, purple non-sulfur bacteria clones have been detected in the Kiritimati hypersaline lake microbial mats, and certainly contribute to inorganic carbon fixation. However, based on the currently available data, there is no clear evidence that these microorganisms may play a crucial role in microbialite formation.

(ii) Sulfate-reduction certainly is a significant process in element cycling in Kiritimati hypersaline microbial mats. Sulfide production is evident in lowermost mat parts, and *Deltaproteobacteria* indeed have been detected in brown flocculent aggregates just below the mats (**Tab. 3, Fig. 11**). In addition, biomarkers detected by Bühring et al. (2009) point to sulfate-reducing bacteria present already in oxic zone of the mats. These may be active in darkness as well as under daylight conditions (Canfield & Des Marais 1991). However, contrary to other metabolic pathways (e.g. oxygenic photosynthesis), the mechanism how sulfate-reducing bacteria affect the carbonate equilibrium is not clear. The sum equation indicates that sulfate-reduction using carbohydrates or organic acids such as acetate increases carbonate alkalinity, which, at constant pH, does only cause a minor rise in CO₃²⁻ activity and hence CaCO₃ mineral supersaturation (Aloisi 2008):



In microbial mats, simultaneous CO₂ release from digestion of organic compounds commonly causes a decrease in pH, and hence decrease in CaCO₃ mineral supersaturation. Certainly, the effect of sulfate reduction is dependent on the electron-donor used in the reaction (e.g., H₂ instead of CH₃COOH or CH₂O; Visscher & Stolz 2005). However, if these electron donors are not supplied from an external

source but from within the mat, their production from organic precursors is linked with CO₂ liberation, so that the sum effect on the carbonate equilibrium is negligible.

Nonetheless, case studies have demonstrated a spatial correlation of sulfate-reducing bacteria and CaCO₃ precipitation (Visscher et al. 2000). However, mechanism of how sulfate-reducing bacteria induced precipitation is currently not fully understood (Baumgartner et al. 2006: 141) and model calculations question the significance of sulfate reduction in inducing CaCO₃ precipitation in these mats (Aloisi 2008). One mechanism suggested by Baumgartner et al. (2006) is the modification of the extracellular polymeric substances through partial degradation by bacteria, especially SRB. However, then, the crucial mechanism is not the process of sulfate-reduction but the exopolymer-digestion by SRB (and other prokaryotes). In any case, detailed studies of exopolymers produced or modified by sulfate-reducing bacteria (Braissant et al. 2007) or other heterotrophic bacteria form a promising field for a clearer understanding of how these microorganisms affect microbialite formation. Apart from that, the effect on the carbonate equilibrium is different, when sulfate-reduction is coupled with other metabolic processes, e.g. Fe³⁺ reduction (Hendry 1993):

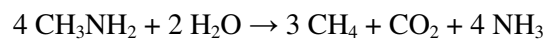


Such coupling might indeed support microbialite formation in settings of sufficient Fe³⁺ supply, e.g. in areas with influx from siliciclastics (e.g., Arp et al. 2008: 1245), or from igneous or metamorphic rocks. However, on the atoll of Kiritimati only carbonate rocks are available for weathering and there is no substantial source of iron (except from former military vehicles). Consequently, iron concentrations in lake and pore waters of Kiritimati lakes are low, and coupling of sulfate reduction with iron reduction is unlikely to occur.

(iii) In contrast, ammonification is substantially involved in the anaerobic decomposition of organic matter in the Kiritimati hypersaline lake microbial mats. This is indicated by high NH₄⁺ concentrations in Lake 21 and 22 porewater samples (**Tab. 1**). Nonetheless, pH values at the grey mat bottom and within porewaters decrease from 7.6 to 7.16. Thus, the sum effect of all microbial processes including ammonification at the mat basis results in a further decrease in CaCO₃ mineral

supersaturation. Again, it seems unlikely that this metabolic process is a crucial factor in microbialite formation in Kiritimati hypersaline lakes.

(iv) The composition of microbial community (**Fig. 9, 10, 11; Tab. 3**) indicates that methanogenesis as well as methylotrophy may play a significant role in the microbialite-forming mats of Kiritimati hypersaline lakes. For cold seep environments it is known that a combination of sulfate-reduction and methanotrophy fuels the formation of CaCO₃ precipitates, which then show significantly ¹³C-depleted stable isotope values (Roberts et al., 1989). Contrary to this, Kiritimati microbialites show ¹³C-enriched, positive δ¹³C values (**Fig. 16**). No external source of methane (seep) is known, and methane is rather produced within the mats. Here, autotrophic methanogenesis could be important in raising pH by CO₂ consumption (Kenward et al. 2009). The identified methanogens in the investigated mats, however, are methylotrophs, and hence do not consume but release CO₂ only, except when using methylamines:



Then, excess of NH₃ release relative to CO₂, and protonation to NH₄⁺ increases pH and hence carbonate activity. Indeed, anoxic porewaters in the investigated lakes are high in NH₄⁺. However, as discussed with respect to other pathways of ammonification, the observed near neutral pH values in pore spaces below the mat bottom argue against a crucial role of methylamine-consuming methanogens.

Further field and laboratory analysis are required to understand why microbialites form in the hypersaline Lakes 2, 21 and 22, but not in the hypersaline Lake 51. Based on current knowledge, one crucial point that may lead to differences in microbial communities and element cycling might be that Lake 51 receives seawater-recharge via a canal-like connection to lagoon, whereas Lakes 2, 21 and 22 have higher Ca²⁺ concentrations due to additional groundwater and/or surface water influx. In particular, night measurements of physicochemical gradients, and analysis of sulfide and methane concentrations and fluxes, and expression of functional genes (cf. Breitbart et al. 2009), e.g. involved in exopolymer degradation, may contribute to resolve these problems.

7. Conclusions

Microbialites with a unique reticulate fabric were discovered below microbial mats in hypersaline lakes on the atoll of Kiritimati. The mats display a clear colour-zonation, with an orange top layer, a green, purple and grey layer below, and a brown flocculent basis. Despite of high oxygenic photosynthesis in top parts of the mat and a high aragonite supersaturation in the water column, microbialite formation takes place in lower, oxic to anoxic mat parts.

The hypersaline lakes are filled by evaporated seawater modified by CaCO_3 and gypsum precipitation. Those lakes hosting microbialites are in addition enriched in Ca^{2+} via surface and/or subsurface influx. The prokaryotic community of the microbial mats is characterized by abundant phylotypes closely related to halotolerant taxa and taxa with preference to oligotrophic habitats. Besides *Cyanobacteria*, which are the major primary producers, *Alphaproteobacteria* (among them purple non-sulphur bacteria), *Betaproteobacteria*, *Gammaproteobacteria*, *Deltaproteobacteria*, *Bacteroidetes*, *Actinobacteria*, *Acidobacteria*, *Spirochaetes*, *Firmicutes*, *Chloroflexi*, *Planctomycetes*, *Crenarchaeota*, *Euryarchaeota*, representatives of the candidate phyla TM6 and OP8, as well as unclassified taxa were detected. Complementary to the methylotrophic genus *Methanohalophilus*, which is likely a dominant methanogen in the basal mat parts, a number of phylotypes throughout the different mat layers parts find their closest known relatives in representatives from methane seep environments. This points to a significant cycling of methane and methyl compounds within the mats. Indeed, stable isotope analyses point to carbonate precipitation from an inorganic carbon pool depleted in ^{12}C , due to photosynthesis and/or methanogenesis.

The microbialite consist of three aragonitic structural components: spherulites, layers and sheets, and fibrous veneers. Spherulites start forming already in orange top parts of the mat, are thus interpreted as a result of extraordinary high photosynthesis overcoming inhibition by pristine exopolymers. Microbial layers and sheets start forming in crevice-like zones of green and purple mat parts, where photosynthesis is still active. Consequently, break-down of exopolymers inhibiting precipitation concurrent to photosynthetic carbon assimilation is considered as key factor in microbialite formation. The final fibrous aragonite veneers may reflect slow syntaxial overgrowth at low supersaturation and

almost lack of inhibiting exopolymers. While sulphate reduction, methylotrophy, methanogenesis and ammonification play an important role in element cycling of the mat, there is currently no evidence for a crucial role in the formation of microbialite in the hypersaline lakes of Kiritimati.

Acknowledgements

We are indebted to the Ministry of Environment and Social Development in Tarawa, Republic of Kiribati for the permission to carry out the study on Kiritimati. The Ministry of Natural Resources Development on Kiritimati, Republic of Kiribati, kindly gave the export permission for the samples. The field trip was supported by Iannang Teaoro, Ministry of Fisheries and Agriculture, Kiritimati, Republic of Kiribati. We are grateful to Farther Bermond (†6. April 2006), Kiritimati, for hospitality, board and lodging. John W. Murphy, AusAID Kiritimati Water Supply and Sanitation Project, kindly provided rainfall data and enabled sampling of groundwater wells. X-ray diffractometry was carried out by Volker Karius, Göttingen. Analysis of stable isotopes was supported by Ingrid Reuber, Göttingen. Erko Stackebrandt, DSMZ Braunschweig, made valuable suggestions on an earlier version of this manuscript. This study is funded by the German Research Foundation, project Re 665/18-2, and Ar 335/5-3 of the Research Unit 571 "Geobiology of Organo- and Biofilms" (DFG-For 571 publication #52). We thank Brian Jones and an anonymous reviewer for their helpful comments and suggestions.

References

- Aloisi G. 2008. The calcium carbonate saturation state in cyanobacterial mats throughout Earth's history. *Geochimica et Cosmochimica Acta* 72: 6037-6060.
- Aloisi G, Bouloubassi I, Heijs SK, Pancost RD, Pierre C, Sinninghe Damsté JS, Gottschal JC, Forney LJ, Rouchy JM. 2002. CH₄-consuming microorganisms and the formation of carbonate crusts at cold seeps. *Earth and Planetary Science Letters* 203: 195-203.

- Altschul SF, Madden TL, Schäffer AA, Zhang J, Zhang Z, Miller W, Lipman DJ. 1997. Gapped BLAST and PSI-BLAST: a new generation of protein database search programs. *Nucleic Acids Research* 25: 3389-3402.
- Anandham R, Indiragandhi P, Madhaiyan M, Chung J, Ryu KY, Jee HJ & Sa T. 2009. Thiosulfate oxidation and mixotrophic growth of *Methylobacterium goesingense* and *Methylobacterium fujisawaense*. *Journal of Microbiology and Biotechnology* 19: 17-22.
- Arp G, Hofmann J, Reitner J. 1998. Microbial Fabric Formation in Spring Mounds ("Microbialites") of Alkaline Salt Lakes in the Badain Jaran Sand Sea, PR China. *Palaios* 13: 581-592.
- Arp G, Thiel V, Reimer A, Michaelis W, Reitner J. 1999. Biofilm exopolymers control microbialite formation at thermal springs discharging into the alkaline Pyramid Lake, Nevada, USA. *Sedimentary Geology* 126: 159-176.
- Arp G, Reimer A, Reitner J. 2001. Photosynthesis-induced biofilm calcification and calcium concentrations in Phanerozoic oceans. *Science* 292: 1701-1704.
- Arp G, Bissett A, Brinkmann N, Cousin S, de Beer D, Friedl T, Mohr KI, Neu TR, Reimer A, Shiraishi F, Stackebrandt E, Zippel B. 2010. Tufa-forming biofilms of German karstwater streams: Microorganisms, exopolymers, hydrochemistry and calcification. *Geological Society Special Publication* 336: 83-118.
- Baumgartner LK, Reid RP, Dupraz C, Decho AW, Buckley DH, Spear JR, Przekop KM, Visscher PT. 2006. Sulfate reducing bacteria in microbial mats: changing paradigms, new discoveries. *Sedimentary Geology* 185: 131-145.
- Bissett A, de Beer D, Schoon R, Shiraishi F, Reimer A, Arp G. 2008. Microbial mediation of stromatolite formation in karst-water creeks. *Limnology & Oceanography* 53: 1159-1168.
- Bosak T, Greene SE, Newmann DK. 2007. A likely role for anoxygenic photosynthetic microbes in the formation of ancient stromatolites. *Geobiology* 5: 119-126.
- Braissant O, Decho AW, Dupraz C, Glunk C, Przekop KM, Visscher PT. 2007 Exopolymeric substances of sulfate-reducing bacteria: Interactions with calcium at alkaline pH and implication for formation of carbonate minerals. *Geobiology* 5: 401-411.

- Breitbart M, Hoare A, Nitti A, Siefert J, Haynes M, Dinsdale E, Edwards R, Souza V, Rohwer F, Hollander D. 2009. Metagenomic and stable isotopic analyses of modern freshwater microbialites in Cuatro Ciénegas, Mexico. *Environmental Microbiology* 11: 16-34.
- Bühning SI, Smittenberg RH, Sachse D, Lipp JS, Golubić S, Sachs JP, Hinrichs KU, Summons RR. 2009. A hypersaline microbial mat from the Pacific Atoll Kiritimati: insights into composition and carbon fixation using biomarker analyses and a ^{13}C -labeling approach. *Geobiology* 7: 1-16.
- Canfield DE, Des Marais DJ. 1991. Aerobic sulfate reduction in microbial mats. *Science* 251: 1471-1473.
- Cavicchioli R, Fegatella F, Ostrowski M, Eguchi M, Gottschal J. 1999. Spingomonads from marine environments. *Journal of Industrial Microbiology & Biotechnology* 23: 268-272.
- Cole JR, Chai B, Marsh TL, Farris RJ, Wang Q, Kulam SA, Chandra S, McGarrell DM, Schmidt TM, Garrity GM, Tiedje JM. 2003. The Ribosomal Database Project (RDP-II): previewing a new autoaligner that allows regular updates and the new prokaryotic taxonomy. *Nucleic Acids Research* 31: 442-443.
- Davidova IA, Harmsen HJM, Stams AJM, Belyaev SS, Zehnder AJB. 1997. Taxonomic description of *Methanococcoides euhalobius* and its transfer to the *Methanohalophilus* genus. *Antonie van Leeuwenhoek* 71: 313-318.
- Défarque C, Trichet J, Jaunet AM, Robert M, Tribble J, Sansone F. 1996. Texture of microbial sediments revealed by cryo-scanning electron microscopy. *Journal of Sedimentary Research* 66: 935-947.
- Denger K, Stackebrandt E, Cook AM 1999. *Desulfonispora thiosulfatigenes* gen. nov., sp. nov., a taurine-fermenting, thiosulfate-producing anaerobic bacterium. *International Journal of Systematic Bacteriology* 49: 1599-1603.
- Dotzauer C, Ehrmann MA, Vogel RF. 2002. *Thermoanaerobacterium* and *Thermoanaerobacter* in canned food. *Food Technology and Biotechnology* 40: 21-26.
- Douthit HA, Pfennig N. 1976. Isolation and growth rates of methanol utilizing Rhodospirillaceae. *Archives of Microbiology* 107: 233-234.

- Dupraz CD, Visscher PT, Baumgartner LK, Reid RP. 2004. Microbe-mineral interactions: early carbonate precipitation in a hypersaline lake (Eleuthera Island, Bahamas). *Sedimentology* 51: 745-765.
- Dupraz C, Reid RP, Braissant O, Decho AW, Norman RS, Visscher PT. 2009. Processes of carbonate precipitation in modern microbial mats. *Earth-Science Reviews* 96: 141-162.
- Fahy A, Ball AS, Lethbridge G, Timmis KN, McGenity TJ. 2008. Isolation of alkali-tolerant benzene-degrading bacteria from a contaminated aquifer. *Letters in Applied Microbiology* 47: 60-66.
- Falkland AC, Woodroffe CD. 1997. Geology and hydrogeology of Tarawa and Kiritimati, Kiribati. *Developments in Sedimentology* 54: 577-610.
- Garrett P. 1970. Phanerozoic stromatolites: noncompetitive ecologic restriction by grazing and burrowing animals. *Science* 169: 171-173.
- Gleave AP, Taylor RK, Morris BA, Greenwood DR. 1995. Cloning and sequencing of a gene encoding the 69-kDa extracellular chitinase of *Janthinobacterium lividum*. *FEMS Microbiology Letters* 131: 279-288.
- Government of Kiribati. 1993. Republic of Kiribati 1:50 000, Sheet Kiritimati (Christmas Island). Series X782 (DOS 436) Edition 8-OS 1993, Ordnance Survey.
- Green PN. 2006. *Methylobacterium*. - In: Dworkin M, Falkow S, Rosenberg E, Schleifer KH, Stackebrandt E, editors. *The Prokaryotes, Volume 5: Proteobacteria: Alpha and Beta Subclasses*. New York: Springer. P 257-265.
- Hendry JP. 1993. Calcite cementation during bacterial manganese, iron and sulphate reduction in Jurassic shallow marine carbonates. *Sedimentology* 40: 87-106.
- Huber T, Faulkner G, Hugenholtz P. 2004. Bellerophon; a program to detect chimeric sequences in multiple sequence alignments. *Bioinformatics* 20: 2317-2319.
- Huber JA, Johnson HP, Butterfield DA, Baross JA 2006. Microbial life in ridge flank crustal fluids. *Environmental Microbiology* 8: 88-99.
- Isenbarger TA, Finney M, Rios-Velazquez C, Handelsman J, Ruvkun G. 2008. Miniprimer PCR, a new lens for viewing the microbial world. *Applied and Environmental Microbiology* 74: 840-849.

- Jones B., Renaut RW. 1996. Morphology and growth of aragonite crystals in hot-spring travertines at Lake Bogoria, Kenya Rift Valley. *Sedimentology* 43: 323-340.
- Kahle C.F. 1994. Facies and evolution of Silurian coral-microbialite reef complex, Maumee, Ohio, USA. *Journal of Sedimentary Research* 64a: 711-725.
- Kempe S., Kazmierczak J. 1990. Calcium carbonate supersaturation and the formation of in situ calcified stromatolites. In: Ittekkot VA, Kempe S, Michaelis W, Spitzzy A, editors. *Facets of Modern Biogeochemistry*. Berlin: Springer. P 255-278.
- Kempe S, Kazmierczak J, Landmann G, Konuk T, Reimer A, Lipp A. 1991. Largest known microbialites discovered in Lake Van, Turkey. *Nature* 349: 605-608.
- Kenward PA, Goldstein RH, González LA, Roberts JA. 2009. Precipitation of low-temperature dolomite from an anaerobic microbial consortium: the role of methanogenic Archaea. *Geobiology* 7: 556-565.
- Komárek J., Anagnostidis K. 1999. Cyanoprokaryota, Teil 1. Chroococcales. In: Ettl H, Gerloff J, Heynig H, Mollenhauer D, editors. *Süßwasserflora von Mitteleuropa*. Heidelberg: Spektrum. Band 19/1. 548 pp.
- Knittel K, Boetius A, Lemke A, Eilers H, Lochte K, Pfannkuche O, Linke P, Amann R. 2003. Activity, distribution, and diversity of sulfate reducers and other bacteria in sediments above gas hydrate (Cascadia Margin, Oregon). *Geomicrobiology Journal* 20: 269-294.
- Lane DJ. 1991. 16S/23S rRNA sequencing. In: Stackebrandt E, Godfellow M, editors. *Nucleic Acid Techniques in Bacterial Systematics*. New York, N.Y.: John Wiley and Sons. P 115-175.
- Lanoil BD, Sassen R, La Duc MT, Sweet ST, Nealson KH. 2001. Bacteria and Archaea physically associated with Gulf of Mexico gas hydrates. *Applied and Environmental Microbiology* 67: 5143-5153.
- Larimer FW, Chain P, Hauser L, Lamerdin J, Malfatti S, Do L, Land ML, Pelletier DA, Beatty JT, Lang AS, Tabita FR, Gibson JL, Hanson TE, Bobst C, Torres y Torres JL, Peres C, Harrison FH, Gibson J, Harwood CS. 2003. Complete genome sequence of the metabolically versatile photosynthetic bacterium *Rhodospseudomonas palustris*. *Nature Biotechnology* 22: 55-61.

- Laval B, Cady SL, Pollack JC, McKay CP, Bird JS, Grotzinger JP, Ford DC, Bohm HR. 2002. Modern freshwater microbialite analogues for ancient dendritic reef structures. *Nature* 407: 626-629.
- Lenke H, Pieper DH, Bruhn C, Knackmuss HJ. 1992. Degradation of 2,4-Dinitrophenol by two *Rhodococcus erythropolis* strains, HL 24-1 and HL 24-2. *Applied and Environmental Microbiology* 58: 2928-2932.
- Lim DSS, Laval BE, Slater G, Antoniadis D, Forrest AL, Pike W, Pieters R, Saffari M, Reid D, Schulze-Makuch D, Andersen D, McKay CP. 2009. Limnology of Pavilion Lake, B. C., Canada – Characterization of a microbialite forming environment. *Fundamental and Applied Limnology* 173: 329-351.
- Liu Y, Boone DR, Choy C. 1990. *Methanohalophilus oregonense* sp. nov. a methylotrophic methanogen from an alkaline, saline aquifer. *International Journal of Systematic Bacteriology* 40: 111-116.
- Lloyd KG, Lapham L, Teske A. 2006. An anaerobic methane-oxidizing community of ANME-1b Archaea in hypersaline Gulf of Mexico sediments. *Applied and Environmental Microbiology* 72: 7218-7230.
- Minz D, Fishbain S, Green SJ, Muyzer G, Cohen Y, Rittmann BE, Stahl D. 1999. Unexpected population distribution in a microbial mat community: Sulfate-reducing bacteria localized to the highly oxic chemocline in contrast to a eukaryotic preference for anoxia. *Applied and Environmental Microbiology* 65: 4659–4665.
- Northrop J. 1962. Geophysical observations on Christmas Island. - *Atoll Research Bulletin* 89: 1-2.
- Orphan VJ, Hinrichs KU, Ussler W III, Paull CK, Taylor LT, Sylva SP, Hayes JM, DeLong EF. 2001. Comparative analysis of methane-oxidizing archaea and sulfate-reducing bacteria in anoxic marine sediments. *Applied and Environmental Microbiology* 67: 1922-1934.
- Orphan VJ, Jahnke LL, Embaye T, Turk KA, Pernthaler A, Summons RE, Des Marais DJ 2008. Characterization and spatial distribution of methanogens and methanogenic biosignatures in hypersaline microbial mats of Baja California. *Geobiology* 6: 376-393.

- Palleroni NJ. 2005. Genus I. *Burkholderia*. In: Garrity GM, editor. Bergey's manual of systematic bacteriology. 2nd ed. Volume 2 The Proteobacteria Part C The Alpha-, Beta-, Delta-, and Epsilonproteobacteria. New York: Springer. P 575-600.
- Parcell W.C. 2002. Sequence stratigraphic controls on the development of microbial fabrics and growth forms-implications for reservoir quality distribution in the Upper Jurassic (Oxfordian) Smackover Formation, eastern Gulf Coast, USA. *Carbonates and Evaporites* 17: 166-181.
- Parkhurst DL, Appelo CAJ 1999. User's guide to PHREEQC (version 2)- a computer program for speciation, batch-reaction, one-dimensional transport, and inverse geochemical calculations. U.S. Geological Survey Water-Resources Investigations Report 99-4259: 1-312.
- Pascual J, Macián MC, Arahal DR, Garay E, Pujalte MJ. 2010. Multilocus sequence analysis of the central clade of the genus *Vibrio* by using the 16S rRNA, *recA*, *pyrH*, *rpoD*, *gyrB*, *rctB* and *toxR* genes. *International Journal of Systematic and Evolutionary Microbiology* 60: 154-165.
- Paterek JR, Smith PH. 1988. *Methanohalophilus mahii* gen. nov., sp. nov., a methylotrophic halophilic methanogen. *International Journal of Systematic Bacteriology* 38: 122-123.
- Pentecost A. 2005. Travertine. Berlin: Springer. 445 p.
- Peters F, Rother M, Boll M. 2004. Selenocysteine-containing proteins in anaerobic benzoate metabolism of *Desulfococcus multivorans*. *Journal of Bacteriology* 186: 2156-2163.
- Pratt B.R. 1982. Stromatolitic framework of carbonate mud-mounds. *Journal of Sedimentary Petrology* 52: 1203-1227.
- Purdy EG, Gischler E. 2005. The transient nature of the empty bucket model of reef sedimentation. *Sedimentary Geology* 175: 35-47.
- Reid RP, Browne KM. 1991. Intertidal stromatolites in a fringing Holocene reef complex, Bahamas. *Geology* 19: 15-18.
- Richert L, Golubić S, Le Guédès R, Hervé A, Payri C. 2006. Cyanobacterial populations that build 'kopara' microbial mats in Rangiroa, Tuamotu Archipelago, French Polynesia. *European Journal of Phycology* 41: 259-279.
- Riding R. 2000. Microbial carbonates: the geological record of calcified bacterial-algal mats and biofilms. *Sedimentology* 47, Supplement 1: 179-214.

- Risatti JB, Capman WC, Stahl DA. 1994. Community structure of a microbial mat: the phylogenetic dimension. *Proceedings of the National Academy of Sciences of the United States of America* 91: 10173-10177.
- Roberts HH, Sassen R, Carney R, Aharon P. 1989. ¹³C-depleted authigenic carbonate buildups from hydrocarbon seeps, Louisiana continental slope. *Gulf Coast Association of Geological Societies Transactions* 39: 523-530.
- Robertson CE, Spear JR, Harris JK, Pace NR. 2009. Diversity and stratification of archaea in a hypersaline microbial mat. *Applied and Environmental Microbiology* 75: 1801-1810.
- Sachse D, Sachs JP. 2008. Inverse relationship between D/H fractionation in cyanobacterial lipids and salinity in Christmas Island saline ponds. *Geochimica et Cosmochimica Acta* 72: 793-806.
- Saenger C, Miller M, Smittenberg RH, Sachs JP. 2006. A physico-chemical survey of inland lakes and saline ponds: Christmas Island (Kiritimati) and Washington (Teraina) Islands, Republic of Kiribati. *Saline Systems* 2006, 2: 8. doi: 10.1186/1746-1448-2-8.
- Sambrook J, Russell DW. 2001. *Molecular Cloning – A Laboratory Manual*. 3rd ed., Cold Spring Harbor: Cold Spring Harbor Laboratory Press. 2344 p.
- Sasikala C., Ramana CV. 1998. Biodegradation and metabolism of unusual carbon compounds by anoxygenic phototrophic bacteria. *Advances in Microbial Physiology* 39: 339-377.
- Shiraishi F, Bissett A, de Beer D, Reimer A, Arp G. 2008a. Photosynthesis, respiration and exopolymer calcium-binding in biofilm calcification (Westerhöfer and Deinschwanger Creek, Germany). *Geomicrobiology Journal* 25: 83-94.
- Shiraishi F, Zippel B, Neu TR, Arp G 2008b. In situ detection of bacteria in calcified biofilms using FISH and CARD-FISH. *Journal of Microbiological Methods* 75: 103-108.
- Stahl DA, Key R, Flesher B, Smit J. 1992. The phylogeny of marine and freshwater *Caulobacter*s reflects their habitat. *Journal of Bacteriology* 174: 2193-2198
- Staley JT, Konopka AE, Dalmasso J.P. 1987. Spatial and temporal distribution of *Caulobacter* spp. in two mesotrophic lakes. *FEMS Microbiology Ecology* 45:1-6.
- Tamura K, Dudley J, Nei M, Kumar S. 2007. MEGA 4: Molecular Evolutionary Genetics Analysis (MEGA) software version 4.0. *Molecular Biology and Evolution* 24: 1596-1599.

- Trichet J, Défarge C, Tribble J, Tribble G, Sansone F. 2001. Christmas Island lagoonal lakes, models for the deposition of carbonate - evaporite - organic laminated sediments. *Sedimentary Geology* 140: 177-189.
- Valencia M. 1977. Christmas Island (Pacific Ocean): reconnaissance geologic observations. *Atoll Research Bulletin* 197: 1-14.
- Van Aken B, Peres CM, Doty SL, Yoon JM, Schnoor JL. 2004. *Methylobacterium populi* sp. nov., a novel aerobic, pink-pigmented, facultatively methylotrophic, methane-utilizing bacterium isolated from poplar trees (*Populus deltoides*x*nigra* DN34). *International Journal of Systematic and Evolutionary Microbiology* 54: 1191-1196.
- Visscher PT, Stolz JF. 2005. Microbial mats as bioreactors: populations, processes, and products. *Palaeogeography, Palaeoclimatology, Palaeoecology* 219: 87-100.
- Visscher PT, Reid RP, Bebout BM. 2000. Microscale observations of sulfate reduction: correlation of microbial activity with lithified micritic laminae in modern marine stromatolites. *Geology* 28: 919-922.
- von Pia J. 1934. Die Kalkbildung durch Pflanzen. Beihefte zum botanischen Zentralblatt A 52: 1-72.
- Widdel F. 1980. Anaerober Abbau von Fettsäuren und Benzoesäure durch neu isolierte Arten. Ph.D. thesis, University of Göttingen, Göttingen. 443 p.
- Winderl C, Anneser B, Griebler C, Meckenstock RU, Lueders T. 2008. Depth-resolved quantification of anaerobic toluene degraders and aquifer microbial community patterns in distinct redox zones of a tar oil contaminant plume. *Applied and Environmental Microbiology* 74: 792-801.
- Winsborough BM, Seeler JS, Golubic S, Folk RL, Maguire B Jr. 1994. Recent fresh-water lacustrine stromatolites, stromatolitic mats and oncoids from Northeastern Mexico. In: Bertrand-Sarfati J., Monty C. editors. *Phanerozoic stromatolites II*. Dordrecht: Kluwer. P 71-100.
- Woodroffe CD, McLean RF. 1998. Pleistocene morphology and Holocene emergence of Christmas (Kiritimati) Island, Pacific Ocean. *Coral Reefs* 17: 235-248.